

Dynamical deconfinement transition driven by density of excitations

Nishan Ranabhat,^{1,2,*} Alessandro Santini,^{1,†} Emanuele Tirrito,^{2,3,‡} and Mario Collura^{1,4,§}

¹*SISSA, via Bonomea 265, 34136 Trieste, Italy*

²*ICTP, Strada Costiera 11, 34151 Trieste, Italy*

³*Pitaevskii BEC Center, CNR-INO and Dipartimento di Fisica, Università di Trento, Via Sommarive 14, Trento, I-38123, Italy*

⁴*INFN, via Bonomea 265, 34136 Trieste, Italy*

(Dated: 18th December 2023)

We investigate the deconfinement transition driven by excitations in long-range spin models. At low temperatures, these models exhibit a confined phase where domain-wall (or kinks) are localized. As temperature increases, kinks interact and propagate, leading to a transition to a de-confined phase. This transition is influenced by the interplay between thermal energy and interaction effects, resulting in extended, de-confined regions. Although kink density is dynamically stable, non-equilibrium changes in their fluctuations characterize the transition. Our findings provide insights into the mechanisms of confinement and deconfinement in long-range spin models, with implications for both condensed matter physics and lattice gauge theories. This study sheds light on the universal aspects of confinement and opens avenues for further exploration and experimental verification.

Introduction: Confinement, as observed in quantum chromodynamics (QCD), is a phenomenon that binds fundamental particles, such as quarks and gluons, into stable heavier particles known as hadrons [1–5]. This binding occurs because of the presence of a confining potential, which asymptotically increases with particle separation. Recent research in lattice gauge theories [6–14] and quantum spin chains [15–21] has explored the effects of confinement in out-of-equilibrium settings, revealing anomalous dynamical behavior that ultimately leads to the suppression of thermalization [6, 22, 23]. Despite the fundamental differences between the lattice gauge theories and quantum spin chains, there is a connection between the observed confinement behavior in these two systems. Notably, the two-dimensional Ising model can exhibit confinement-like behavior, similar to that observed in lattice gauge theories [24–26]. Therefore, the study of simplified magnetic spin models can provide valuable insights into the mechanisms of confinement and phase transitions in complex gauge theories.

In recent years, there has been increasing interest in the study of confinement-deconfinement transitions in lattice gauge theories [12, 27–35] and quantum spin chains [16–18, 36, 37]. This interest arises from the direct analogy between this behavior and the confinement-deconfinement crossover hypothesized in QCD, where stable hadrons transform into quark-gluon plasma at extremely high energy densities. In particular, the ferromagnetic long-range Ising model (LRIM) with power-law decaying interactions has been a paradigmatic model for such investigations because long-range ferromagnetic interactions naturally induce confinement and localize domain-wall kinks to specific regions of the lattice [15, 16]. These bound-domain wall kinks are analogous to stable hadrons in QCD.

In this study, we explore the confinement-deconfinement transition in the long-range Ising

model, driven by the density of excitations that has been adjusted by temperature. In a previous study for short range confined Ising chain it was observed that rare events with mesons created in close proximity lead to an avalanche of scattering events which give rise to a stable prethermal regime [38]. Here, we begin with a thermal state with non-trivial kink density that is tuned by the temperature followed by a quench to the confining phase of the long-range Ising model [16, 17, 37]. We investigate the real-time dynamics of the average kink density and kink fluctuation [17, 19].

We employ state-of-the-art tensor network simulations [39–41] to represent the thermal states as matrix density operators (MPDO) [42–44] and simulate their subsequent real-time evolution. The post-quench real-time dynamics of a mixed density matrix exhibit a much richer behavior compared to that of a pure state with a non-zero density of kinks. Both the average kink density and kink fluctuation show strong signatures of transition from a low-temperature strongly confined phase to a high-temperature deconfined phase. Finally, we employ an effective semi-classical model with a single kink [15] to theoretically predict the observed confinement-deconfinement transition. Our results can be experimentally realized using various Atomic, Molecular, and Optical (AMO) platforms [17, 45–52] which are capable of implementing the global quench protocol.

Model: We study a spin-1/2 ferromagnetic long-range Ising model (LRIM) under open boundary conditions, described by the following Hamiltonian:

$$\hat{H}(J, \alpha, h) = -J \sum_{i < j} \frac{\hat{\sigma}_i^x \hat{\sigma}_j^x}{|i - j|^\alpha} - h \sum_{i=1}^N \hat{\sigma}_i^z \quad (1)$$

Here, σ_i^ν represents the Pauli matrix in the i^{th} site

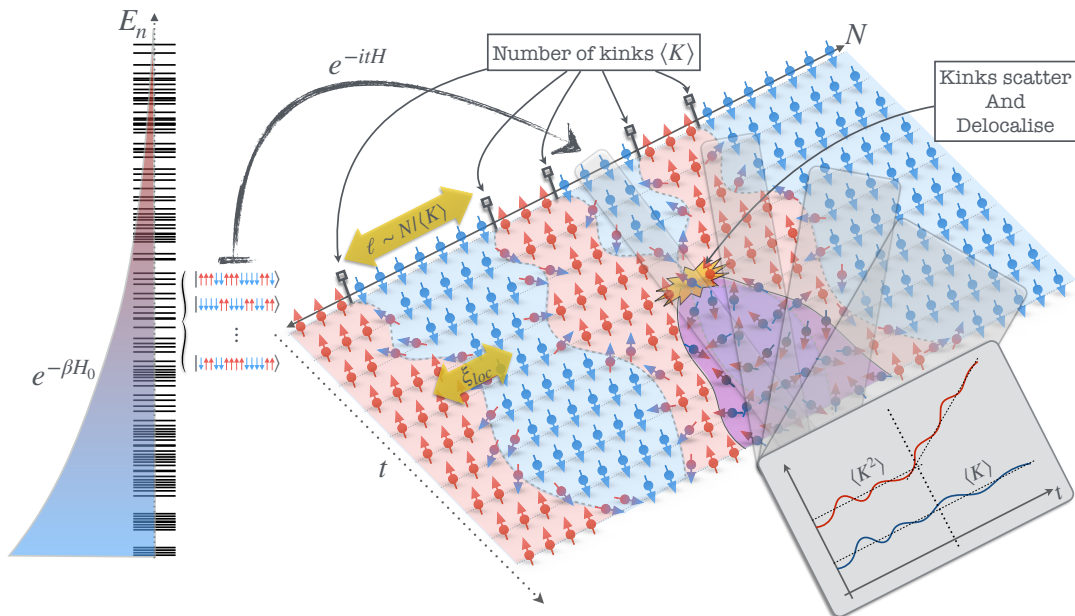


Figure 1. Schematic diagram of the quench protocol: **1)** Initial states are prepared as thermal density matrices of the initial Hamiltonian, $\propto e^{-\beta \hat{H}_0}$ at varying temperatures ($\beta = 1/T$). **2)** The initial thermal density matrix is evolved in real time with a final Hamiltonian $\propto e^{-it\hat{H}}$. Here, we illustrate the evolution of a single representative state with a thermal density matrix. $\langle K \rangle$ is the average number of domain wall kinks, l is the average distance between two kinks and ξ_{loc} is the localization length defined as the maximum distance traced by a domain wall kink. **3)** We probe the real time evolution by calculating the kink density and kink fluctuation at every time step.

and ν^{th} directions. The long-range interaction between the two spins follows an inverse power law of their separation distance, controlled by the parameter α . The transverse magnetic field h governs the kinetic term in the Hamiltonian. We adopt an energy scaling convention with J set to 1. The LRIM demonstrates integrable behavior at the two extremities of α . At $\alpha = \infty$, it simplifies to the nearest-neighbor transverse field Ising model (TFIM) and can be effectively solved by mapping onto spinless fermions through the Jordan-Wigner transformation [53]. Conversely, when $\alpha = 0$, it transforms into a fully connected model [54–56]. TFIM exhibits a quantum phase transition between the ferromagnetic and paramagnetic phases at $h = J$, which persists for all values of α with an increasing critical point [57–59]. Additionally, at $\alpha \leq 2$ we observe a thermal phase transition in the LRIM from a low-temperature ferromagnetic phase to a high-temperature paramagnetic phase [60, 61]. In recent years, LRIM has emerged as a paradigmatic spin model for studying non-equilibrium physics in many-body systems owing to its rich array of intriguing features, including dynamical phase transitions [45, 46, 56, 62–66], prethermalization phenomena [22, 23], nonlinear lightcone propagation [67, 68], and the emergence of time crystals [69, 70]. Furthermore, LRIM exhibits the phenomenon of dynamical confinement, wherein it confines domain wall kinks into bound

quasiparticles, ultimately resulting in the suppression of information propagation within the system [15–17, 37].

Quench dynamics: We initialize our states as a thermal density matrix $\hat{\rho}_\beta(t=0) \propto e^{-\beta \hat{H}_0}$, where β represents the inverse temperature and the initial Hamiltonian \hat{H}_0 has a zero magnetic field. The initial states evolve in real time with the post-quench Hamiltonian $\hat{\rho}_\beta(t+dt) = e^{-idt\hat{H}} \hat{\rho}_\beta(t) e^{idt\hat{H}}$ (see figure 1). The post-quench Hamiltonian parameters are selected to reside within the strongly confined regime [15, 16]. The thermal state is simulated as a mixed density matrix in a locally purified form [42, 43]. We begin at an infinite temperature, that is, $\beta = 0$ where the state is maximally entangled and has a trivial representation as the matrix product density operator (MPDO) [42]. We obtain subsequent finite temperature states by the imaginary time evolution of the maximally mixed state [71]. The thermal states realized as MPDO are then evolved in real time. We employ a two-site time dependent variational algorithm (TDVP) [72, 73] with second order integration scheme for both imaginary and real time evolution of MPDO [71]. The elementary excitations during real-time dynamics are domain wall kinks, which propagate through the system in real time spreading correlation. Consequently, kink density emerges as a natural order parameter for investigating confinement and its impact on correlation

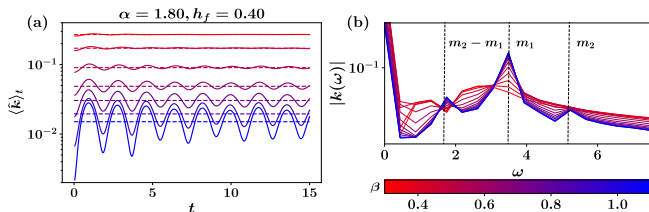


Figure 2. **(a)** Time evolution of kink density following a quench to $\alpha = 1.8$, $h_f = 0.4$, system is initialized at $\alpha = 1.8$, $h_i = 0.0$ at different temperatures. The horizontal dashed lines represent the kink densities of the thermal states corresponding to the quenches. The results are for system size of $N = 50$ spins. **(b)** Fourier spectrum of $\langle \hat{k} \rangle_t$ (right panel). The vertical dashed lines corresponds to the meson masses calculated from the effective two kink model [71]. The colorbar is common to both panels.

propagation within the system [15–18]. Specifically, it is defined as

$$\hat{k} = \frac{1}{N} \sum_{i=1}^{N-1} \frac{1 - \hat{\sigma}_i^x \hat{\sigma}_{i+1}^x}{2}, \quad (2)$$

quantifying the number of nearest neighbor kinks within the system. The initial state is represented by a mixed thermal density matrix, with the average kink density ranging from 0.5 at infinite temperature (corresponding to a maximally mixed state) to 0 at lower temperatures ([71]). Therefore, the parameter β serves as a tuning parameter to precisely control the initial state of the system with varying kink densities.

In Figure 2 **(a)**, we plot the post-quench evolution of the average kink density, $\langle \hat{k} \rangle_t$, initiated from various initial thermal states within a temperature range $0.30 \leq \beta \leq 1.10$. The horizontal dashed lines represent the expected thermal values $\text{Tr}[\hat{\rho}_{\tilde{\beta}} \hat{k}]$, where $\hat{\rho}_{\tilde{\beta}} \propto e^{-\tilde{\beta} \hat{H}}$ and the effective temperature attributed to a quench [74] $\tilde{\beta}$ is extracted by solving the equation,

$$\frac{\text{Tr}[\hat{\rho}_{\tilde{\beta}} \hat{H}_0]}{\text{Tr}[\hat{\rho}_{\tilde{\beta}}]} = \frac{\text{Tr}[\hat{\rho}_{\tilde{\beta}} \hat{H}]}{\text{Tr}[\hat{\rho}_{\tilde{\beta}}]} \quad (3)$$

We observe two distinct behaviors at the extremities of the investigated temperature range. At lower temperatures, the kink density persistently oscillates around the expected thermal value with no signs of relaxation. This is indicative of strong confinement and suppression of the correlation spreading within the system and eventual delay of thermalization [75]. This behavior weakens as the temperature increases, and at high temperatures, the kink density rapidly relaxes to the expected thermal value, suggesting robust thermalization [75] and deconfinement [16, 18]. Figure 2 **(b)** shows the Fourier spectrum of $\langle \hat{k} \rangle_t$. At lower temperatures we observe sharp frequency peaks

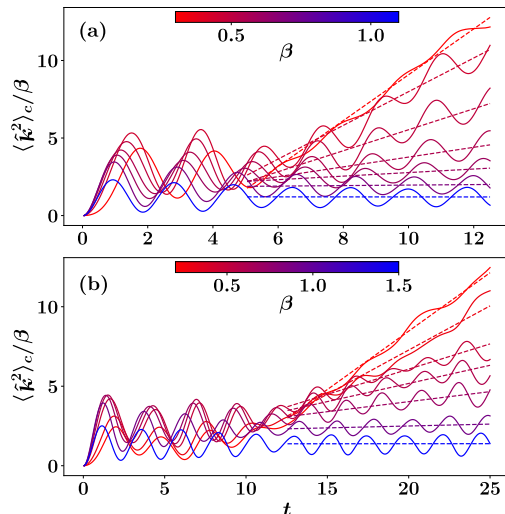


Figure 3. Time evolution of the kink fluctuation at different temperatures (the color bar shows the inverse temperature β) for $\alpha = 1.8, h_f = 0.4$ **(a)** and $\alpha = 2.3, h_f = 0.4$ **(b)**. The results are for system size of $N = 50$ spins. The data are rescaled by $1/\beta$ and subtracted from their initial values for better visualization. Dashed lines represent the linear fit of the data in an appropriate time window.

corresponding to the dominant oscillations of $\langle \hat{k} \rangle_t$. These frequency peaks exhibit strong agreement with the meson masses extracted from the two-kink model [15, 16, 18, 19, 37] (refer to [71] for additional details) indicative of the presence of strongly bound mesons. However, as the temperature increases, these frequency peaks gradually diminish and ceases to exist, indicating the dissolution of bound mesons at high temperature [76].

Evolution of kink fluctuation: Kink density provides valuable qualitative insights into the deconfinement transition, revealing distinct behaviors at the extreme ends of the temperature range under examination. However, a more prominent signature of this transition emerges from the interaction and propagation of domain wall kinks within the system. To address this, we study the connected kink fluctuation $\langle \hat{k}^2 \rangle_c = \langle \hat{k}^2 \rangle - \langle \hat{k} \rangle^2$.

In Figure 3, we depict the post-quench evolution of $\langle \hat{k}^2 \rangle_c$ for two distinct sets of post-quench parameters. For both post-quench Hamiltonians, we observe two contrasting behaviors at the extremes of the temperature range considered. At lower temperatures, $\langle \hat{k}^2 \rangle_c$ exhibits persistent oscillations over time, similar to the behavior of $\langle \hat{k} \rangle_t$, indicating a significant suppression in the propagation of domain wall kinks. As the temperature increases, $\langle \hat{k}^2 \rangle_c$ exhibits linear growth over time, suggesting a light-cone-like dispersion of the domain wall kinks. This observation aligns with light-cone spreading of correlation and entanglement in the deconfined phase, as previously discussed in the literature [15, 16, 18]. A more compre-

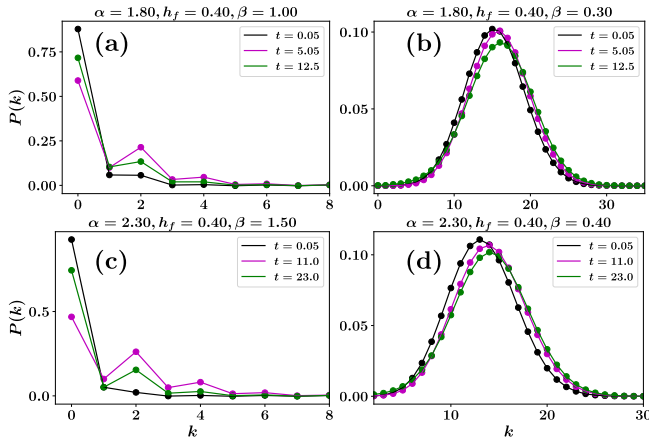


Figure 4. Probability distribution function (PDF) of domain wall kinks for different system parameters and temperature. Three colors represent different time slices during the real time dynamics (see label). (a) and (c) exhibits strong confinement at low temperature with persistent oscillation of PDF, (b) and (d) exhibits high temperature deconfinement where the PDF consistently gets broader with time (see [71] for details on calculation of $P(k)$)

hensive understanding emerges when we examine the full probability distribution $P(k)$ of the domain wall kinks. In Figure 4 (b) and (d), we observe that $P(k)$ monotonically broadens over time, whereas in Figure 4 (a) and (c), it exhibits oscillations in time. To quantitatively assess this behavior, we fit straight lines to the $\langle \hat{k}^2 \rangle_c$ data over an appropriate time window and define the slope of these lines as the velocity of kink dispersion v . In figure 5 we plot v as the function of temperature of the initial thermal states. We observe a transition from a strongly confined regime at low temperatures denoted by $v \approx 0$ to a de-confined regime denoted by a monotonically increasing finite v as the temperature increases. This monotonic rise in v halts eventually because of the finite size effects.

The underlying mechanism of this transition can be understood by studying the dynamics of an effective single kink model, previously employed to study the quasi-localized excitations and suppression of transport in one-dimensional spin chains [15, 77]. The semi-classical limit of the single kink model is given by the Hamiltonian,

$$H_{\alpha,h,N}^{\text{cls}}(k, q) = V_{\alpha,N}(q) - 2h \cos(k) \quad (4)$$

where,

$$V_{\alpha,N}(q) = \frac{2[q^{2-\alpha} + (N-q)^{2-\alpha} - (N-1)^{2-\alpha}]}{(\alpha-1)(2-\alpha)}, \quad (5)$$

and $(k, q) \in [0, 2\pi] \times [1, N-1]$ [71]. Within this framework we define the localization length for a given system

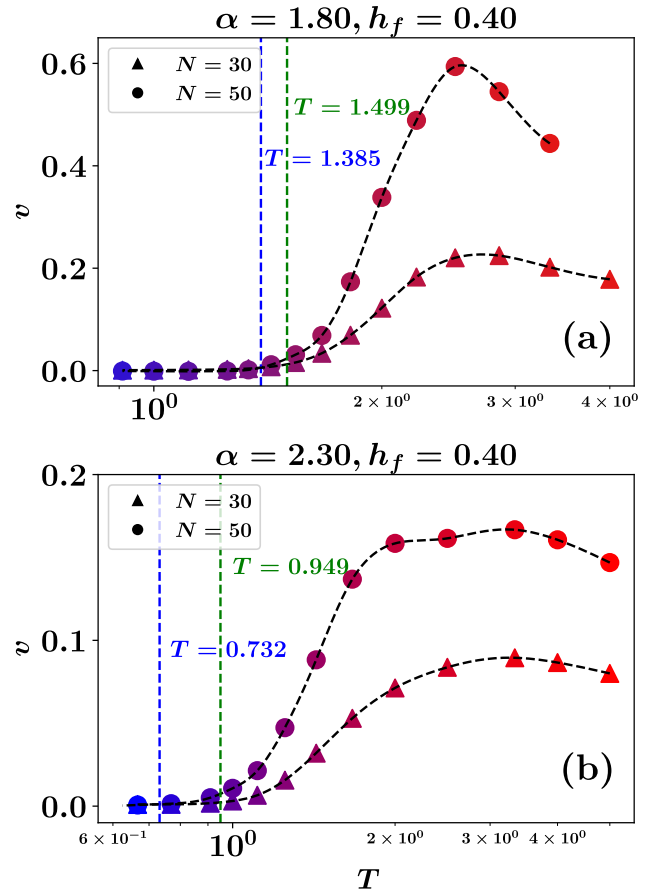


Figure 5. Velocity of kink fluctuation extracted from 3 as a function temperature for two different quenches: $\alpha = 1.8, h_f = 0.4$ (a) and $\alpha = 2.3, h_f = 0.4$ (b) and system sizes $N = 30$ (solid triangle) and $N = 50$ (solid circle). The color gradient represents varying temperature. Dashed black lines are for visual guidance. Horizontal dashed lines are the deconfinement transition temperatures predicted by the single kink model: blue for $N = 50$, green for $N = 30$.

parameters, ξ_{loc} as the maximum distance traced by the single kink initialized at rest with the maximum possible energy that is by solving for maximum q in the equation,

$$H_{\alpha,N}^{\text{cls}}(0, N/2) = H_{\alpha,N}^{\text{cls}}(k, q). \quad (6)$$

ξ_{loc} provides a natural threshold for deconfinement transition. If the separation between kinks is larger than localization length, $l = 1/\langle \hat{k} \rangle \gg \xi_{loc}$ the kinks undergo persistent Bloch oscillations localized at their site of origin, however when $1/\langle \hat{k} \rangle \lesssim \xi_{loc}$, kinks scatter and delocalize, effectively destroying confinement [38]. We can extract the corresponding transition temperature by solving the following equation for β ,

$$\frac{1}{\xi_{loc}} = \overline{\langle \hat{k}_\beta(t) \rangle}, \quad (7)$$

where $\overline{\langle \hat{k}_\beta(t) \rangle}$ is the time averaged $\text{Tr}[\hat{\rho}_\beta(t)\hat{k}]$. It is apparent from Figure 2 that $\overline{\langle \hat{k}_\beta(t) \rangle} = \text{Tr}[\hat{\rho}_\beta\hat{k}]$ holds true for all values of β . By substituting this relation into Equation 7, the transition temperature can be determined numerically. In Figure 5, the dashed horizontal lines represent the deconfinement transition temperatures obtained using this method. Despite the simplicity of the single-kink model, it demonstrates a strong predictive capacity for transition temperature.

This observation can be realized in trapped-ion experiments and other Atomic, Molecular, and Optical (AMO) platforms [17, 45–52] that are capable of initiating the global quench protocol from an initial product state. The post-quench evolution of a mixed state can be realized by independently evolving individual pure states within the given mixed state and subsequently computing the weighted ensemble average of the individual pure state evolution: $\hat{\rho}_\beta(0) \rightarrow \hat{\rho}_\beta(t) = \sum_n P_\beta(n) |n(t)\rangle \langle n(t)|$, where $|n(t)\rangle = e^{-it\hat{H}} |n\rangle$ and $P_\beta(n) = e^{-\beta E_n} / \sum_n e^{-\beta E_n}$. State $|n\rangle$ represents the eigenstate of \hat{H}_0 , and E_n corresponds to the associated eigenvalue. Notably, this procedure scales exponentially with the system size. However, for practical purposes, it is feasible to consider only the dominant states, based on how $P_\beta(n)$ decays with n . This is particularly applicable to low-temperature states.

Conclusion: We have studied the out-of-equilibrium dynamics of thermal states following a global quantum quench to a confined phase of a long-range Ising model [15–17]. The post-quench time evolution of domain walls kinks and their Fourier signals have highlighted the intricate interplay between slow-decaying long-range interactions and the emergence of confinement-like behavior at low temperature. Furthermore, the time dependent fluctuation of domain wall kinks provides a solid evidence of dynamical deconfinement transition with increasing initial kink density that has been tuned thermally.

Our study opens up promising avenues for both theoretical exploration and experimental verification. The identification of the initial density as a key parameter influencing the deconfinement transition offers a new direction for experimental investigations in various AMO platforms [17, 45–52]. Moreover, the implications of our results extend beyond the regime of condensed matter physics, resonating with the study of confinement in lattice gauge theories [6–12].

Acknowledgements: We acknowledge discussion with Guido Pagano regarding experimental realization of our work in trapped-ion platform. We also acknowledge Alvise Bastianello for fruitful discussion regarding the theoretical aspects of confinement and thermalization. E.T. acknowledge support from the MIUR Programme FARE (MEPH), and from QUANTERA DYNAMITE PCI2022-132919. M.C. acknowledge support from the PNRR MUR project PE0000023-NQSTI and by the

PRIN 2022 (2022R35ZBF) - PE2 - “ManyQLowD”.

* nranabha@sissa.it

† asantini@sissa.it

‡ emanuele.tirrito@unitn.it

§ mcollura@sissa.it

- [1] P. Coleman, *Introduction to many-body physics* (Cambridge University Press, 2015).
- [2] W. Greiner, S. Schramm, and E. Stein, *Quantum chromodynamics* (Springer Science & Business Media, 2007).
- [3] W. Busza, K. Rajagopal, and W. Van Der Schee, *Annual Review of Nuclear and Particle Science* **68**, 339 (2018).
- [4] J. Berges, M. P. Heller, A. Mazeliauskas, and R. Venugopalan, *Reviews of Modern Physics* **93**, 035003 (2021).
- [5] A. Rothkopf, *Physics Reports* **858**, 1 (2020).
- [6] T. Chanda, J. Zakrzewski, M. Lewenstein, and L. Tagliacozzo, *Phys. Rev. Lett.* **124**, 180602 (2020).
- [7] R. D. Sedgewick, D. J. Scalapino, and R. L. Sugar, *Phys. Rev. B* **65**, 054508 (2002).
- [8] S. Kühn, E. Zohar, J. I. Cirac, and M. C. Bañuls, *Journal of High Energy Physics* **2015**, 10.1007/jhep07(2015)130 (2015).
- [9] T. Pichler, M. Dalmonte, E. Rico, P. Zoller, and S. Montangero, *Phys. Rev. X* **6**, 011023 (2016).
- [10] E. Zohar, J. I. Cirac, and B. Reznik, *Phys. Rev. Lett.* **109**, 125302 (2012).
- [11] J. C. P. Barros, M. Dalmonte, and A. Trombettoni, *Phys. Rev. D* **100**, 036009 (2019).
- [12] G. Magnifico, M. Dalmonte, P. Facchi, S. Pascazio, F. V. Pepe, and E. Ercolessi, *Quantum* **4**, 281 (2020).
- [13] W.-Y. Zhang, Y. Liu, Y. Cheng, M.-G. He, H.-Y. Wang, T.-Y. Wang, Z.-H. Zhu, G.-X. Su, Z.-Y. Zhou, Y.-G. Zheng, *et al.*, arXiv preprint arXiv:2306.11794 (2023).
- [14] J. C. Halimeh, I. P. McCulloch, B. Yang, and P. Hauke, *PRX Quantum* **3**, 040316 (2022).
- [15] A. Leroze, B. Žunkovič, A. Silva, and A. Gambassi, *Phys. Rev. B* **99**, 121112 (2019).
- [16] F. Liu, R. Lundgren, P. Titum, G. Pagano, J. Zhang, C. Monroe, and A. V. Gorshkov, *Phys. Rev. Lett.* **122**, 150601 (2019).
- [17] W. L. Tan, P. Becker, F. Liu, G. Pagano, K. S. Collins, A. De, L. Feng, H. B. Kaplan, A. Kyprianidis, R. Lundgren, W. Morong, S. Whitsitt, A. V. Gorshkov, and C. Monroe, *Nature Physics* **17**, 742747 (2021).
- [18] M. Kormos, M. Collura, G. Takács, and P. Calabrese, *Nature Physics* **13**, 249246 (2017).
- [19] J. Vovrosh and J. Knolle, *Sci Rep* **11**, 11577 (2021).
- [20] G. Lagnese, F. M. Surace, M. Kormos, and P. Calabrese, *Phys. Rev. B* **104**, L201106 (2021).
- [21] G. Lagnese, F. M. Surace, M. Kormos, and P. Calabrese, *Journal of Physics A: Mathematical and Theoretical* **55**, 124003 (2022).
- [22] J. C. Halimeh, V. Zauner-Stauber, I. P. McCulloch, I. de Vega, U. Schollwöck, and M. Kastner, *Phys. Rev. B* **95**, 024302 (2017).
- [23] B. Neyenhuis, J. Zhang, P. W. Hess, J. Smith, A. C. Lee, P. Richerme, Z.-X. Gong, A. V. Gorshkov, and C. Monroe, *Science Advances* **3**, 10.1126/sciadv.1700672 (2017).
- [24] A. A. Belavin, A. M. Polyakov, and A. B. Zamolodchikov, *Journal of Statistical Physics* **34**, 763 (1984).

- [25] M. Henkel and H. Saleur, *Journal of Physics A: Mathematical and General* **22**, L513 (1989).
- [26] P. Fonseca and A. Zamolodchikov, arXiv preprint hep-th/0612304 (2006).
- [27] M. Kebrič, J. C. Halimeh, U. Schollwöck, and F. Grusdt, Confinement in 1+1d \mathbb{Z}_2 lattice gauge theories at finite temperature (2023), arXiv:2308.08592 [cond-mat.quant-gas].
- [28] B. Buyens, J. Haegeman, F. Hebenstreit, F. Verstraete, and K. Van Acoleyen, *Phys. Rev. D* **96**, 114501 (2017).
- [29] B. Buyens, J. Haegeman, H. Verschelde, F. Verstraete, and K. Van Acoleyen, *Phys. Rev. X* **6**, 041040 (2016).
- [30] E. Ercolessi, P. Facchi, G. Magnifico, S. Pascazio, and F. V. Pepe, *Phys. Rev. D* **98**, 074503 (2018).
- [31] E. A. Martinez, C. A. Muschik, P. Schindler, D. Nigg, A. Erhard, M. Heyl, P. Hauke, M. Dalmonte, T. Monz, P. Zoller, *et al.*, *Nature* **534**, 516 (2016).
- [32] J. Park, Y. Kuno, and I. Ichinose, *Phys. Rev. A* **100**, 013629 (2019).
- [33] M. Aidelsburger, L. Barbiero, A. Bermudez, T. Chanda, A. Dauphin, D. González-Cuadra, P. R. Grzybowski, S. Hands, F. Jendrzejewski, J. Jünemann, *et al.*, *Philosophical Transactions of the Royal Society A* **380**, 20210064 (2022).
- [34] O. Băzăvan, S. Saner, E. Tirrito, G. Araneda, R. Srinivas, and A. Bermudez, arXiv preprint arXiv:2305.08700 (2023).
- [35] J. Mildenberger, W. Mruczkiewicz, J. C. Halimeh, Z. Jiang, and P. Hauke, arXiv preprint arXiv:2203.08905 (2022).
- [36] M. C. Banuls, M. P. Heller, K. Jansen, J. Knaute, and V. Svensson, A quantum information perspective on meson melting (2022), arXiv:2206.10528 [hep-th].
- [37] S. Scopa, P. Calabrese, and A. Bastianello, *Physical Review B* **105**, 125413 (2022).
- [38] S. Birnkammer, A. Bastianello, and M. Knap, *Nature Communications* **13**, 7663 (2022).
- [39] U. Schollwöck, *Annals of physics* **326**, 96 (2011).
- [40] R. Orús, *Annals of physics* **349**, 117 (2014).
- [41] S.-J. Ran, E. Tirrito, C. Peng, X. Chen, L. Tagliacozzo, G. Su, and M. Lewenstein, *Tensor network contractions: methods and applications to quantum many-body systems* (Springer Nature, 2020).
- [42] F. Verstraete, J. J. García-Ripoll, and J. I. Cirac, *Phys. Rev. Lett.* **93**, 207204 (2004).
- [43] A. H. Werner, D. Jaschke, P. Silvi, M. Kliesch, T. Calarco, J. Eisert, and S. Montangero, *Phys. Rev. Lett.* **116**, 237201 (2016).
- [44] D. Jaschke, S. Montangero, and L. D. Carr, *Quantum Science and Technology* **4**, 013001 (2018).
- [45] J. Zhang, G. Pagano, P. W. Hess, A. Kyprianidis, P. Becker, H. Kaplan, A. V. Gorshkov, Z.-X. Gong, and C. Monroe, *Nature* **551**, 601 (2017).
- [46] P. Jurcevic, H. Shen, P. Hauke, C. Maier, T. Brydges, C. Hempel, B. P. Lanyon, M. Heyl, R. Blatt, and C. F. Roos, *Phys. Rev. Lett.* **119**, 080501 (2017).
- [47] R. Blatt and C. Roos, *Nature* **8**, 277–284 (2012).
- [48] M. Knap, A. Kantian, T. Giamarchi, I. Bloch, M. D. Lukin, and E. Demler, *Phys. Rev. Lett.* **111**, 147205 (2013).
- [49] J. Zeiher, J.-y. Choi, A. Rubio-Abadal, T. Pohl, R. van Bijnen, I. Bloch, and C. Gross, *Phys. Rev. X* **7**, 041063 (2017).
- [50] H. Bernien, S. Schwartz, A. Keesling, and et al., *Nature* **551**, 579–584 (2017).
- [51] P. Richerme, Z. Gong, A. Lee, and et al., *Nature* **511**, 198–201 (2014).
- [52] J. Britton, B. Sawyer, A. Keith, and et al., *Nature* **484**, 489–492 (2012).
- [53] E. Lieb, T. Schultz, and D. Mattis, *Annals of Physics* **16**, 407 (1961).
- [54] B. Žunkovič, A. Silva, and M. Fabrizio, *Phil. Trans. R. Soc. A* **374**, 10.1098/rsta.2015.0160 (2016).
- [55] A. Das, K. Sengupta, D. Sen, and B. K. Chakrabarti, *Phys. Rev. B* **74**, 144423 (2006).
- [56] N. Ranabhat and M. Collura, *SciPost Phys.* **12**, 126 (2022).
- [57] M. Knap, A. Kantian, T. Giamarchi, I. Bloch, M. D. Lukin, and E. Demler, *Phys. Rev. Lett.* **111**, 147205 (2013).
- [58] T. Koffel, M. Lewenstein, and L. Tagliacozzo, *Phys. Rev. Lett.* **109**, 267203 (2012).
- [59] S. Fey and K. P. Schmidt, *Phys. Rev. B* **94**, 075156 (2016).
- [60] A. Dutta and J. K. Bhattacharjee, *Phys. Rev. B* **64**, 184106 (2001).
- [61] E. Gonzalez-Lazo, M. Heyl, M. Dalmonte, and A. Angelone, *SciPost Phys.* **11**, 76 (2021).
- [62] B. Žunkovič, M. Heyl, M. Knap, and A. Silva, *Phys. Rev. Lett.* **120**, 130601 (2018).
- [63] J. C. Halimeh and V. Zauner-Stauber, *Phys. Rev. B* **96**, 134427 (2017).
- [64] R. Khasseh, A. Russomanno, M. Schmitt, M. Heyl, and R. Fazio, *Phys. Rev. B* **102**, 014303 (2020).
- [65] I. Homrighausen, N. O. Abeling, V. Zauner-Stauber, and J. C. Halimeh, *Phys. Rev. B* **96**, 104436 (2017).
- [66] J. Lang, B. Frank, and J. C. Halimeh, *Phys. Rev. B* **97**, 174401 (2018).
- [67] M. Foss-Feig, Z.-X. Gong, C. W. Clark, and A. V. Gorshkov, *Phys. Rev. Lett.* **114**, 157201 (2015).
- [68] A. S. Buyskikh, M. Fagotti, J. Schachenmayer, F. Essler, and A. J. Daley, *Phys. Rev. A* **93**, 053620 (2016).
- [69] A. Kyprianidis, F. Machado, W. Morong, P. Becker, K. Collins, D. ELSE, L. Feng, P. Hess, C. Nayak, G. Pagano, N. Yao, and C. Monroe, *Science* **372**, 1192 (2021).
- [70] J. Zhang, P. W. Hess, A. Kyprianidis, P. Becker, A. Lee, J. Smith, G. Pagano, I. D. Potirniche, A. C. Porter, A. Vishwanath, N. Y. Yao, and C. Monroe, *Nature* **543**, 217 (2017).
- [71] See supplemental material.
- [72] J. Haegeman, J. I. Cirac, T. J. Osborne, I. Pižorn, H. Verschelde, and F. Verstraete, *Phys. Rev. Lett.* **107**, 070601 (2011).
- [73] J. Haegeman, C. Lubich, I. Oseledets, B. Vandereycken, and F. Verstraete, *Phys. Rev. B* **94**, 165116 (2016).
- [74] F. H. L. Essler and M. Fagotti, *Journal of Statistical Mechanics: Theory and Experiment* **2016**, 064002 (2016).
- [75] M. C. Bañuls, J. I. Cirac, and M. B. Hastings, *Phys. Rev. Lett.* **106**, 050405 (2011).
- [76] M. C. Banuls, M. P. Heller, K. Jansen, J. Knaute, and V. Svensson, A quantum information perspective on meson melting (2022), arXiv:2206.10528 [hep-th].
- [77] P. P. Mazza, G. Peretto, A. Leroze, M. Collura, and A. Gambassi, *Phys. Rev. B* **99**, 180302 (2019).
- [78] J. Eisert, M. Cramer, and M. B. Plenio, *Rev. Mod. Phys.* **82**, 277 (2010).
- [79] M. Srednicki, *Phys. Rev. Lett.* **71**, 666 (1993).

- [80] M. B. Plenio, J. Eisert, J. Dreißig, and M. Cramer, Phys. Rev. Lett. **94**, 060503 (2005).
- [81] P. Calabrese and J. Cardy, Journal of Statistical Mechanics: Theory and Experiment **2004**, P06002 (2004).
- [82] G. Vidal, J. I. Latorre, E. Rico, and A. Kitaev, Phys. Rev. Lett. **90**, 227902 (2003).

Supplemental Materials

TWO KINK MODEL

We use the two kink model to study the low energy excitations as bound quasiparticles in the long-range Ising model. The idea is to project the Hilbert space into a subspace where n spins are clustered together in the sea of up spins, forming two kink domain walls that are free to shift, contract, or expand. The state is defined by two quantum numbers,

$$|j, n\rangle = |\dots \uparrow\uparrow\downarrow_j\downarrow_{j+1} \dots \downarrow\downarrow_{j+n-1}\uparrow\uparrow \dots\rangle \quad (8)$$

The long-range Hamiltonian 1 can be projected in the in the two kink subspace is $\hat{\mathcal{H}} = \hat{\mathcal{P}}^{-1}\hat{H}\hat{\mathcal{P}}$, where $\hat{\mathcal{P}}$ is the projection operator,

$$\hat{\mathcal{H}}|j, n\rangle = V_{\alpha, N}(j, n)|j, n\rangle - h[|j, n+1\rangle + |j, n-1\rangle + |j+1, n-1\rangle + |j-1, n+1\rangle] \quad (9)$$

where, for a finite system with N spins, $1 \leq j \leq N-1$ and $1 \leq n \leq N-j-1$. The first term is diagonal, $V_{\alpha, N}(j, n)$ is the total potential energy above the ground state (fully polarized), and the second off-diagonal term is the spin flip term, which is responsible for the shift, expansion, and contraction of the domain wall kinks. The projected Hamiltonian 9 can be diagonalized on the basis $\{|j, n\rangle\}$ and the masses of the mesons can be extracted from the energy spectrum. The matrix we need to diagonalize is

$$\mathcal{H}_{j, n: j', n'} = V_{\alpha, N}(j, n)\delta_{j, j'}\delta_{n, n'} - h[\delta_{j, j'}\delta_{n+1, n'} + \delta_{j, j'}\delta_{n-1, n'} + \delta_{j+1, j'}\delta_{n-1, n'} + \delta_{j-1, j'}\delta_{n+1, n'}] \quad (10)$$

where,

$$V_{\alpha, N}(j, n) = 2 \sum_{j \leq u \leq j+n-1} \left[\sum_{1 \leq v \leq j-1} \frac{1}{|v-u|^\alpha} + \sum_{j+n \leq v \leq N} \frac{1}{|v-u|^\alpha} \right] \quad (11)$$

is the potential energy of excitation of the two kink states $|j, n\rangle$ above the ground state. This model provides a good description of confinement in a long-range Ising chain in the limit $N \rightarrow \infty$ where the confining potential increases monotonically with distance between the coupled domain walls. However, for a finite spin chain, the confining potential increases with the separation of the kinks up to a characteristic length, after which it starts to decrease. This behavior is more severe for smaller α so the energy spectrum of equation 9 does not provide a good prediction for the masses of the mesons as α is decreased.

SINGLE KINK MODEL AND LOCALIZATION LENGTH

Similar to the two kink model we can define the single kink model by projecting the Hilbert space into a subspace with just one single kink. The quantum state is defined by a single quantum number signifying the position of the single kink,

$$|j, n\rangle = |\dots \uparrow\uparrow\uparrow_n\downarrow_{n+1}\downarrow\downarrow \dots\rangle. \quad (12)$$

The corresponding Hamiltonian is defined as,

$$\mathcal{H}_{n: n'} = V_{\alpha, N}(n)\delta_{n, n'} - h[\delta_{n+1, n'} + \delta_{n-1, n'}] \quad (13)$$

where the effective potential is,

$$V_{\alpha, N}(n) = 2 \sum_{1 \leq i \leq n} \sum_{n+1 \leq j \leq N} \frac{1}{|i-j|^\alpha}. \quad (14)$$

In thermodynamic limit the sums in the potential can be approximated with integrals,

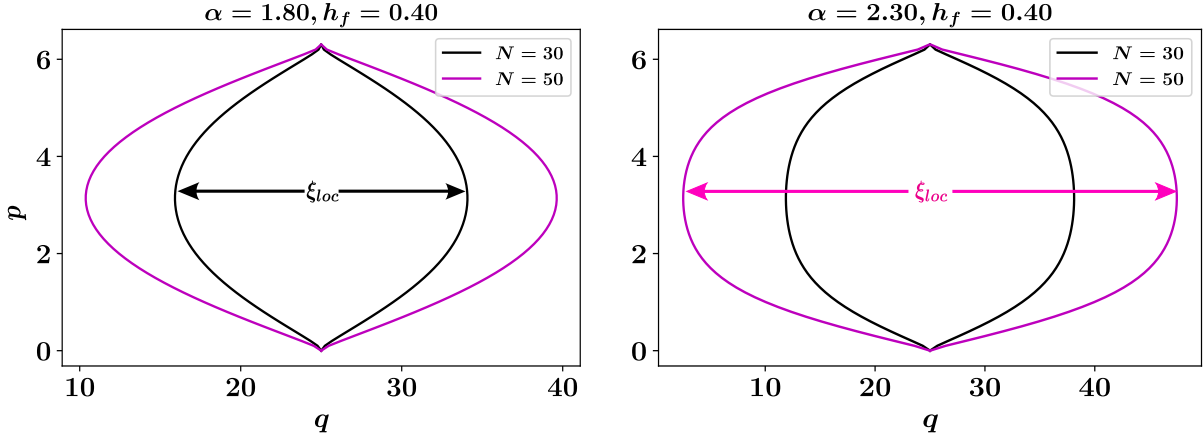


Figure 6. Phase space of the semi-classical Hamiltonian 20 over a full period of momentum for two different system parameters. ξ_{loc} is called the localization length and is defined as the maximum space traversed by the single kink originally located at the center of the system.

$$V_{\alpha,N}(n) = 2 \left[\sum_{r=1}^{N-n} \frac{1}{r^\alpha} + \sum_{r=2}^{N-n+1} \frac{1}{r^\alpha} + \dots + \sum_{r=n}^{N-1} \frac{1}{r^\alpha} \right] \quad (15)$$

$$\approx \left[\int_1^{N-n} \frac{dr}{r^\alpha} + \int_2^{N-n+1} \frac{dr}{r^\alpha} + \dots + \int_n^{N-1} \frac{dr}{r^\alpha} \right] \quad (16)$$

$$= \frac{1}{(\alpha-1)} \left[\sum_{r=1}^n \frac{1}{r^{\alpha-1}} - \sum_{n'=n}^1 \frac{1}{(N-n')^{\alpha-1}} \right] \quad (17)$$

On further approximation of the sums we get,

$$V_{\alpha,N}(n) \approx \frac{2}{(\alpha-1)} \left[\int_1^n \frac{dr}{r^{\alpha-1}} - \int_n^1 \frac{dn'}{(N-n')^{\alpha-1}} \right] \quad (18)$$

$$= \frac{2}{(\alpha-1)(2-\alpha)} \left[\frac{1}{n^{\alpha-2}} + \frac{1}{(N-n)^{\alpha-2}} - 1 - \frac{1}{(N-1)^{\alpha-2}} \right] \quad (19)$$

We can take the classical limit of the Hamiltonian in equation 13 by defining a phase space $(p, q) \in [0, 2\pi] \times [1, N-1]$ and corresponding Hamiltonian,

$$H_{\alpha,h,N}^{\text{cls}}(p, q) = V_{\alpha,N}(q) - 2h \cos(p) \quad (20)$$

where the function $V_{\alpha,N}(q)$ is defined in the equations 19. Starting from the most energetic state in a finite chain within the single kink scenario; a single static kink located at the centre of the chain, we can calculate the $p \times q$ phase space by solving;

$$H_{\alpha,N}^{\text{cls}}(0, N/2) = H_{\alpha,N}^{\text{cls}}(p, q) \quad (21)$$

In figure 6 we plot the classical phase space by solving 21 over a full periodicity of the momentum. We observe that the kink travels farthest from its original position at $p = \pi$. We define this distance as the localization length of the kink, ξ_{loc} . Localization length separates two different dynamical regimes: when the average separation between the kinks is larger than ξ_{loc} the kinks exhibit uncorrelated Bloch oscillations strictly localized at their site of origin, as the average kink separation between kinks becomes comparable to and smaller than ξ_{loc} the kinks disperse and delocalize. The critical temperature corresponding to this transition can be extracted by numerically solving the following equation for β ;

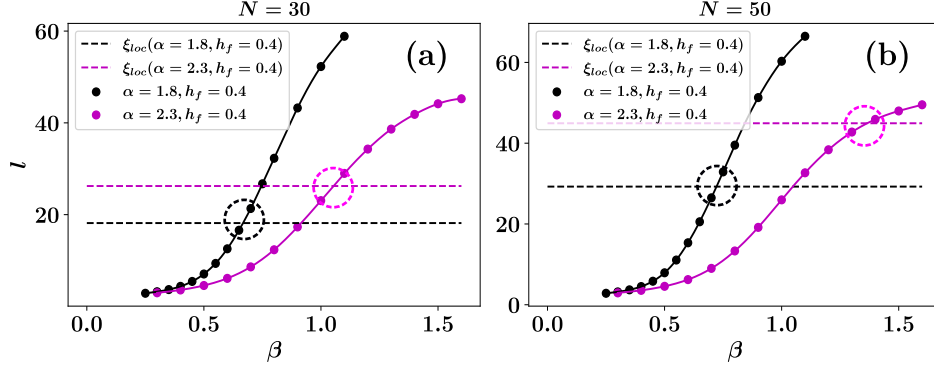


Figure 7. Numerical solution of the equation 22. The dots are the average kink separation, $l = \frac{N}{\text{Tr}[\hat{\rho}_\beta \hat{k}]}$, as a function of β , the full lines are the cubic interpolation of the data, and the horizontal dashed lines are ξ_{loc} for the corresponding parameters. The dashed circles highlights the point of solution.

$$l = \frac{N}{\langle \hat{k}_\beta(t) \rangle} = \xi_{loc}, \quad (22)$$

where $\overline{\langle \hat{k}_\beta(t) \rangle}$ is the time average of $\text{Tr}[\hat{\rho}_\beta(t) \hat{k}]$. The post-quench behavior of $\langle \hat{k}_\beta(t) \rangle$ suggests that we can replace $\langle \hat{k}_\beta(t) \rangle$ with the expected thermal kink density $\text{Tr}[\hat{\rho}_\beta \hat{k}]$.

SIMULATION DETAILS

Simulation of finite temperature states

The finite temperature states are simulated by the method of purification. We begin at infinite temperature, $\beta = 0$, where the state is maximally mixed and can be written as the tensor product of local identities $\hat{\rho}_0 = \bigotimes_{i=1}^N \mathbf{1}^{\sigma_i, \bar{\sigma}_i} = \mathbb{1}$, where $\mathbf{1}^{\sigma_i, \bar{\sigma}_i} = [\delta_{\sigma_i, \bar{\sigma}_i}]_{d \times d}$ and d is the dimension of the physical space. The density operator for any non-zero β is

$$\hat{\rho}_\beta \propto e^{-\beta \hat{H}} = e^{-\frac{\beta}{2} \hat{H}} \mathbb{1} e^{-\frac{\beta}{2} \hat{H}} \quad (23a)$$

$$\propto e^{-\frac{\beta}{2} \hat{H}} \hat{\rho}_0 e^{-\frac{\beta}{2} \hat{H}} \quad (23b)$$

We keep the density operator in locally purified form $\hat{\rho} = \mathbf{X} \mathbf{X}^\dagger$ at each stage where \mathbf{X} is represented as tensor

$$\mathbf{X}_{k_1, k_2, \dots, k_i, \dots, k_N}^{\sigma_1, \sigma_2, \dots, \sigma_i, \dots, \sigma_N} = A_{m_0, m_1}^{\sigma_1, k_1} A_{m_1, m_2}^{\sigma_2, k_2} \dots A_{m_{i-1}, m_i}^{\sigma_i, k_i} \dots A_{m_{N-1}, m_N}^{\sigma_N, k_N} \quad (24)$$

where $s_i = d$, $k_i = d$ are the physical index and the Kraus index are fixed through out and $1 \leq m_i \leq \chi_{max}$ is the bond index. The density operator can now be purified to a given β in trotterized steps

$$\hat{\rho}_{\beta+d\beta} = e^{-\frac{d\beta}{2} \hat{H}} \hat{\rho}_\beta e^{-\frac{d\beta}{2} \hat{H}} \quad (25a)$$

$$= e^{-\frac{d\beta}{2} \hat{H}} \mathbf{X}_\beta \mathbf{X}_\beta^\dagger e^{-\frac{d\beta}{2} \hat{H}} \quad (25b)$$

$$= e^{-\frac{d\beta}{2} \hat{H}} \mathbf{X}_\beta [e^{-\frac{d\beta}{2} \hat{H}} \mathbf{X}_\beta]^\dagger \quad (25c)$$

The simulation of Equation (25) can be achieved through an imaginary time Time-Dependent Variational Principle (TDVP) by employing the transformation $-idt \rightarrow -d\beta$, while rigorously maintaining the locally purified form. It is sufficient to simulate $\mathbf{X}_{\beta+d\beta} = e^{-\frac{d\beta}{2} \hat{H}} \mathbf{X}_\beta$; the other half is a trivial conjugate. We employ a two-site TDVP algorithm with a time step of $d\beta = 0.001$. The initial state, denoted by $\hat{\rho}_0$, is maximally mixed and has a small bond dimension of two. Notably, unlike real-time evolution, the bond dimension does not exhibit excessive growth during imaginary time evolution.

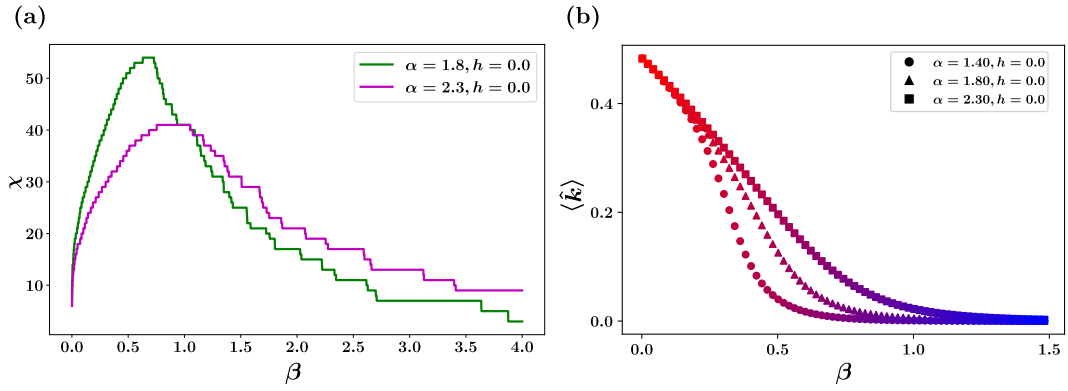


Figure 8. (a) Bond dimension corresponding to the central site as a function of inverse temperature during the imaginary time evolution. All singular values smaller than 10^{-8} are discarded during truncation. (b) Average kink density $\langle \hat{k} \rangle$ as a function of inverse temperature β for three different parameters and system size $N = 51$. The figure illustrates a thermal phase transition from low temperature ferromagnetic regime (in blue) to high temperature paramagnetic regime (in red) based on the kink density. Notice that at $\beta = 0$ kink density is 0.5 for all parameter values which is the expected value for a maximally mixed state. Note: In thermodynamic limit we should not observe a thermal phase transition for $\alpha > 2$, the transition observed here for $\alpha = 2.3, h = 0.0$ is an artifact of finite size effect.

In Figure 8 (a), the bond dimension corresponding to the central site is plotted against β . Truncation involves discarding all singular values smaller than 10^{-8} . The peaks in the plot indicate critical regions where the area law is invalid [78–82]. In Figure 8 (b), the average kink density $\langle \hat{k} \rangle$ is plotted as a function of the inverse temperature β for different α and $h = 0.0$. At $\beta = 0$, the state is maximally mixed and $\langle \hat{k} \rangle = 0.5$ holds for all parameters. As β increases, there is a monotonic reduction in $\langle \hat{k} \rangle$, indicating a thermal transition into the ferromagnetic phase, where $\langle \hat{k} \rangle = 0$. It is important to note that the thermal phase transition observed in Figure 8 is robust only for $\alpha \leq 2$ in the long-range Ising model, and the transition observed for $\alpha = 2.3$ is an artifact of the finite-size effects.

Real time evolution of thermal state

The thermal density operator can be evolved in real time while keeping the locally purified form intact,

$$\hat{\rho}_\beta(t + dt) = e^{-idt\hat{H}} \hat{\rho}_\beta(t) e^{idt\hat{H}} \quad (26a)$$

$$= e^{-idt\hat{H}} \mathbf{X}_\beta(t) \mathbf{X}_\beta^\dagger(t) e^{idt\hat{H}} \quad (26b)$$

$$= e^{-idt\hat{H}} \mathbf{X}_\beta(t) \left[e^{-idt\hat{H}} \mathbf{X}_\beta(t) \right]^\dagger \quad (26c)$$

We employ a two-site Time-Dependent Variational Principle (TDVP) algorithm with a time step of $dt = 0.05$ for real-time evolution. Similar to the imaginary time evolution, it is sufficient to simulate $\mathbf{X}_\beta(t + dt) = e^{-idt\hat{H}} \mathbf{X}_\beta(t)$ with the other half being its trivial conjugate. To assess the convergence of the TDVP data, we calculate the relative error in kink density using three increasing bond dimensions ($\chi_{\max} = 80, 100, 128$) at $\beta = 0.3$, as illustrated in Figure 9. Relative errors consistently remain below $O(10^{-3})$.

The explanation for choosing $\beta = 0.3$ to test the convergence of all TDVP data is straightforward. Increasing the temperature facilitates correlation spreading through the system during real-time evolution, necessitating a higher bond dimension to capture the dynamics effectively. Thus, testing the convergence of errors for the worst-case scenario, where $\beta = 0.3$ is sufficient for our study. The results discussed in the main text are based on a maximum bond dimension of $\chi_{\max} = 128$.

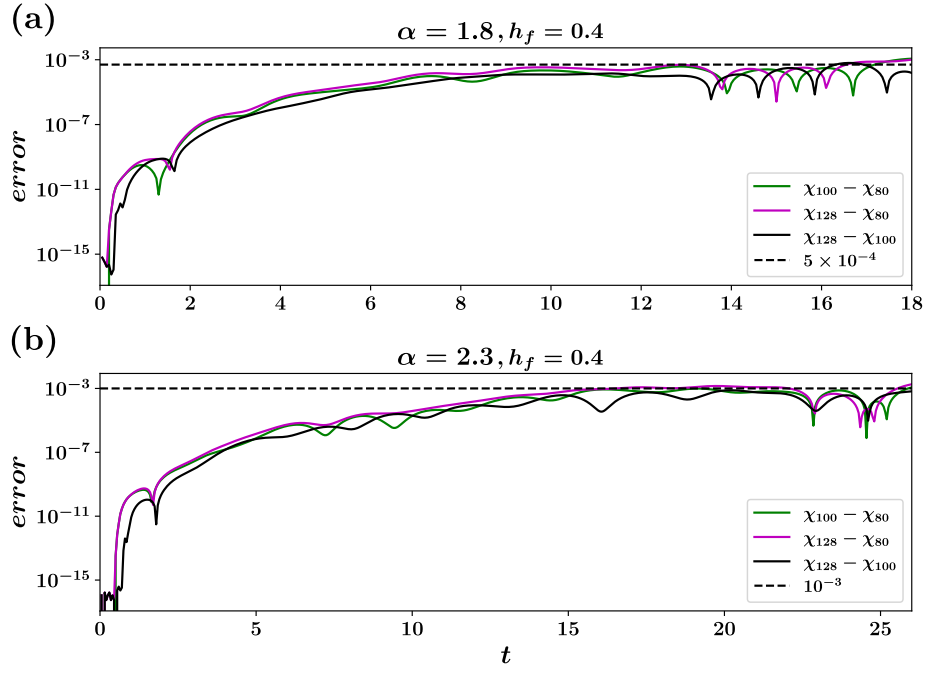


Figure 9. Convergence of the TDVP data for $DT(t)$ with increasing bond dimensions, $\chi = 80, 100, 128$, for $\alpha = 1.8, h_f = 0.4$ (a) and $\alpha = 2.3, h_f = 0.4$ (b). The black dashed line is for visual guidance.

Full counting statistics of kink density

The full counting statistics of a generic quantum mechanical operator \hat{O} over a density matrix $\hat{\rho}$ can be calculated as;

$$P(o) = \text{Tr}[\hat{\rho}\delta(\hat{O} - o)] \quad (27)$$

which can be Fourier transformed to an integral

$$P(o) = \int_{-\infty}^{\infty} \frac{d\theta}{2\pi} e^{-i\theta o} \text{Tr}[\hat{\rho} e^{i\theta \hat{O}}]. \quad (28)$$

In our specific case the operator is the kink density \hat{k} defined in equation 2, replacing this in equation 28 gives us,

$$P(k) = \int_{-\infty}^{\infty} \frac{d\theta}{2\pi} e^{-i\theta \left[k - \frac{N-1}{2} \right]} \text{Tr} \left[\hat{\rho} \prod_{j=1}^{N-1} e^{-i\theta \frac{\hat{\sigma}_j^x \hat{\sigma}_{j+1}^x}{2}} \right]. \quad (29)$$

The problem boils down to calculating the trace of the product of two site exponential operator. We can expand the two site exponential operator by Taylor series and rearrange to break it down into a product of two single site operators acting on site i and $i + 1$ respectively,

$$e^{-i\theta \frac{\hat{\sigma}_j^x \hat{\sigma}_{j+1}^x}{2}} = \cos\left(\frac{\theta}{2}\right) - i \sin\left(\frac{\theta}{2}\right) \hat{\sigma}_j^x \hat{\sigma}_{j+1}^x = \left[\cos\left(\frac{\theta}{2}\right) \mathbb{I}_j \quad -i \sin\left(\frac{\theta}{2}\right) \hat{\sigma}_j^x \right] \begin{bmatrix} \mathbb{I}_{j+1} \\ \hat{\sigma}_{j+1}^x \end{bmatrix} \quad (30)$$

Equation 30 suggests that that the integral in equation 29 has a periodicity of 2π so the integral can be restricted to $\theta \in [-\pi, \pi]$. We reshape and redefine the operators acting on site i and $i + 1$ in equation 30 as MPO_{left} and $\text{MPO}_{\text{right}}$ respectively (see (a) and (b) in figure 10). Each site now has two single site tensors that can be compressed together into a four legged MPO (see (c) in figure 10) which can act on a matrix product density operator in a straight forward manner.

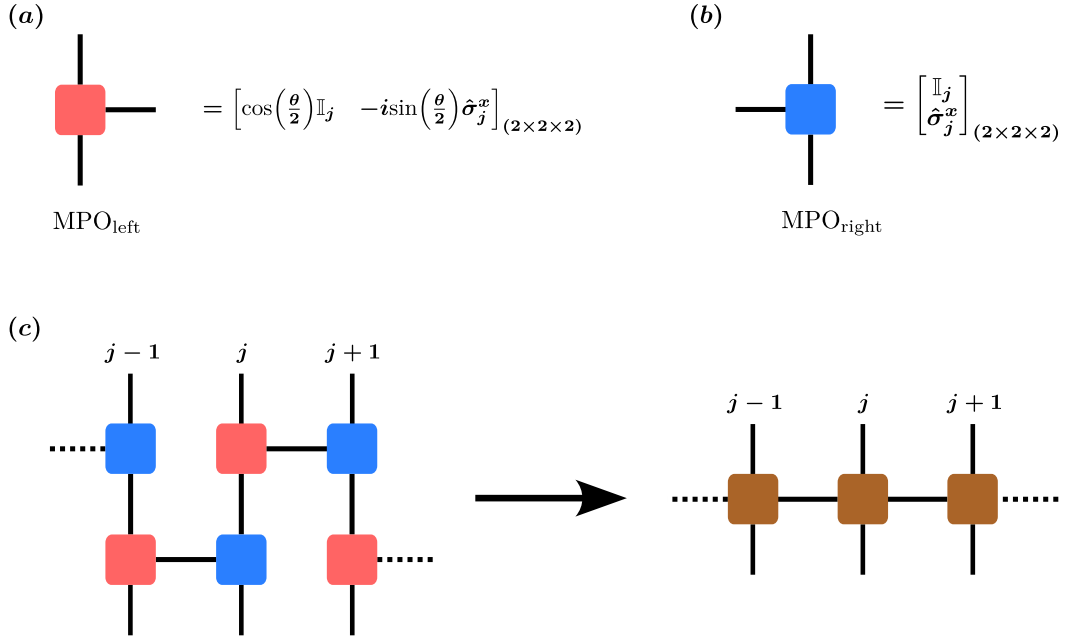


Figure 10. Left (red) and right (blue) MPO at site j , (a) and (b) respectively. Contracting left and right MPO at each site to build a four legged MPO (black) at each site, (c).